Scaling Function, Spectral Function and Nucleon Momentum Distribution in Nuclei

Scaling function, spectral function, and nucleon momentum distribution in nuclei

A. N. Antonov,[1] M. V. Ivanov,[1,2] J. A. Caballero,[3] M. B. Barbaro,[4] J. M. Udias,[2] E. Moya de Guerra,[2] and T. W. Donnelly[5]

[1]*Institute for Nuclear Research and Nuclear Energy, Bulgarian Academy of Sciences, BG-1784 Sofia, Bulgaria*

[2]*Grupo de Física Nuclear, Departamento de Física Atómica, Molecular y Nuclear, Facultad de Ciencias Físicas, Universidad Complutense de Madrid, E-28040 Madrid, Spain*

[3]*Departamento de Física Atómica, Molecular y Nuclear, Universidad de Sevilla, E-41080 Sevilla, Spain*

[4]*Dipartimento di Fisica Teorica, Università di Torino and INFN, Sezione di Torino, Via P. Giuria 1, I-10125 Torino, Italy*

[5]*Center for Theoretical Physics, Laboratory for Nuclear Science and Department of Physics, Massachusetts Institute of Technology, Cambridge, Massachusetts 02139, USA*

(Received 14 December 2010; revised manuscript received 11 March 2011; published 29 April 2011)

The link between the scaling function extracted from the analysis of (e, e') cross sections and the spectral function/momentum distribution in nuclei is revisited. Several descriptions of the spectral function based on the independent particle model are employed, together with the inclusion of nucleon correlations, and effects of the energy dependence arising from the width of the hole states are investigated. Although some of these approaches provide rough overall agreement with data, they are not found to be capable of reproducing one of the distinctive features of the experimental scaling function, namely its asymmetry. However, the addition of final-state interactions, incorporated in the present study using either relativistic mean-field theory or via a complex optical potential, does lead to asymmetric scaling functions in accordance with data. The present analysis seems to indicate that final-state interactions constitute an essential ingredient and are required to provide a proper description of the experimental scaling function.

DOI: 10.1103/PhysRevC.83.045504 PACS number(s): 25.30.Fj, 24.10.Jv, 21.60.Cs, 21.10.Ft

I. INTRODUCTION

Investigations of inclusive quasielastic (QE) electron-nucleus scattering make it possible to obtain information about one of the main characteristics of nuclear structure, namely, the spectral function $S(p, \mathcal{E})$ and its integral, the nucleon momentum distribution $n(p)$ in nuclei [1–3]. This provides insights into the validity of the mean-field approximation (MFA) and the role of the nucleon-nucleon (*NN*) correlations, as well as into the effects of final-state interactions (FSI) for inclusive electroweak processes. Using the shell model, it is possible, in principle, to obtain the contributions of different shells to $S(p, \mathcal{E})$ and the momentum distribution for each single-particle state. However, due to the residual interactions, the hole states are not eigenstates of the residual nucleus but are mixtures of several single-particle states. This leads to the spreading of the shell structure and only a careful study of the momentum dependence of $S(p, \mathcal{E})$ can separate the contributions from different shells [4]. Such analyses have been carried out for few-body systems, complex nuclei, and nuclear matter and have focused mainly on the existence of high-momentum components of the nucleon momentum distribution due to *NN* correlation effects [2–7]. Since it is impossible within the MFA to describe simultaneously the density and momentum distributions in nuclei [4,7–12], a consistent analysis of the role of the *NN* correlations is required using theoretical methods that go beyond the MFA to obtain a successful description of the relevant experiments. The present study uses the results found from studies of y scaling [1–3,13–15] and superscaling (based on ψ-scaling variable) [15–23] obtained from analyses of inclusive electron scattering data. The latter consists in constructing a "superscaling function" $f(\psi)$ obtained by removing the single-nucleon content from the double-differential cross section and plotting it versus a scaling variable $\psi(q, \omega)$. Scaling of the first kind of scaling function [i.e., no explicit q dependence of $f(\psi)$] can be seen at excitation energies below the QE peak. Scaling of second kind [i.e., no dependence of $f(\psi)$ on the mass number] turns out to be excellent in the same region. When scaling of both the first and second type occurs, one says that superscaling has taken place. It was pointed out [18,20–23] that the physical reason for the superscaling is the specific high-momentum tail of $n(p)$, which arises due to *NN* correlations and is similar for all nuclei. As was pointed out in Ref. [24], however, a direct connection between the scaling function, extracted from the analysis of the cross-section data, and the spectral function only exists when one makes very restrictive approximations. Along this line, caution should be kept in mind for the conclusions reached about the momentum distribution, because a close relationship between the latter and the scaling function also only emerges after some approximations are made. In particular, these are linked to the integration limits involved and the behavior of the spectral function [1]. In Ref. [24], the analysis applied in the past to the scaling region (that is, negative values of the scaling variable y) was extended to positive y, leading to results that differ from those based solely on the scaling region and providing new insights into the issue of how the energy and momentum are distributed in the spectral function.

Under certain approximations (see Ref. [24] and references therein), in the Plane-Wave Impulse Approximation (PWIA), the $(e, e'N)$ differential cross section factorizes in the form:

$$\left[\frac{d\sigma}{d\epsilon' d\Omega' dp_N d\Omega_N}\right]^{\mathrm{PWIA}}_{(e,e'N)} = K\sigma^{eN}(q, \omega; p, \mathcal{E}, \phi_N)S(p, \mathcal{E}), \tag{1}$$

where σ^{eN} is the electron-nucleon cross section for a moving off-shell nucleon, $S(p,\mathcal{E})$ is the spectral function that gives the probability to find a nucleon of certain momentum and energy in the nucleus [25–27], and K is a kinematical factor [28]. In Eq. (1), p is the missing momentum and $\mathcal{E}$ is the excitation energy that is essentially the missing energy minus the separation energy. Further assumptions are necessary [24] to show how the scaling function $F(q,\omega)$ emerges from the PWIA, namely, the spectral function is assumed to be isospin independent and σ^{eN} is assumed to have a very mild dependence on p and $\mathcal{E}$. The scaling function can be expressed in terms of the differential cross section for inclusive QE (e,e') processes:

$$F(q,\omega) \cong \frac{[d\sigma/d\epsilon' d\Omega']_{(e,e')}}{\overline{\sigma}^{eN}(q,\omega;\, p=|y|,\, \mathcal{E}=0)}\,, \tag{2}$$

where $\overline{\sigma}^{eN}$ represents the azimuthal angle-averaged single-nucleon cross section that also incorporates the kinematical factor K:

$$\overline{\sigma}^{eN} \equiv K \sum_{i=1}^{A} \int d\phi_{N_i} \frac{\sigma^{eN_i}}{2\pi}.$$

Note that in Eq. (2), $\overline{\sigma}^{eN}$ is taken at $p=|y|$, where the magnitude of the scaling variable y is the smallest value of the missing momentum p that can occur in the process of electron-nucleus scattering for the smallest possible value of the excitation energy ($\mathcal{E}=0$), i.e., at the smallest value of the missing energy. Accordingly, in the PWIA, the scaling function $F(q,\omega)$ from Eq. (2) may be expressed in terms of the spectral function:

$$F(q,\omega) = 2\pi \iint_{\Sigma(q,\omega)} p\, dp\, d\mathcal{E}\, S(p,\mathcal{E})\,, \tag{3}$$

where $\Sigma(q,\omega)$ represents the kinematically allowed region [24]. Only in the case when it is possible to extend the region $\Sigma(q,\omega)$ to infinity in the excitation energy plane (i.e., at $\mathcal{E}_{\max}\to\infty$) would the scaling function be directly linked to the momentum distribution of the nuclear system:

$$n(p) = \int_0^\infty d\mathcal{E} S(p,\mathcal{E}). \tag{4}$$

It was shown from the analyses of the inclusive electron-nucleus scattering that at high values of the momentum transfer the extracted scaling function $F_{\rm expt}(q,\omega)$ becomes a function only of the scaling variable y and not of q [1,17–19]. It was emphasized in [24] that Eq. (3) does not apply to $F_{\rm expt}(q,\omega)$ because of ingredients not included in the PWIA, such as final-state interactions, meson-exchange currents (MEC), rescattering processes, etc.

Using the relativistic Fermi-gas model (RFG) as a guide, the separate analysis of longitudinal (L) and transverse (T) (e,e') data made it possible to introduce three "universal" experimental dimensionless superscaling functions:

$$f_{\rm expt}(q,\omega) \equiv k_A F_{\rm expt}(q,\omega); \quad f^{L(T)}_{\rm expt}(q,\omega) \equiv k_A F^{L(T)}_{\rm expt}(q,\omega)\,, \tag{5}$$

k_A being a phenomenological characteristic momentum scale for the specific nucleus being studied; this is equal to the Fermi momentum k_F in the case of the RFG. In the present work, we consider only the longitudinal scaling function and henceforth drop the subscript "L" for simplicity. Note that the effects of FSI and relativity on this function are often important and, as emphasized in Ref. [24], any conclusion about the momentum distribution based on Eq. (3) should be made with caution.

In the present work, we study in more detail the relationship between the spectral function $S(p,\mathcal{E})$ and the scaling function $F(q,y)$. Our aim is to extract more information about the spectral function from the experimentally known scaling function, keeping in mind the restrictions of the PWIA. We take into account the effects of FSI and some other peculiarities of electron-nucleus scattering. We make an attempt to construct a spectral function that corresponds to the experimentally established scaling function following a series of steps on increasing complexity. First, we construct $S(p,\mathcal{E})$ within and beyond the independent particle shell model (IPSM). Second, we take into account FSI by computing the inclusive electron-nucleus cross section using the Dirac optical potential. We incorporate these results in the determination of the spectral function and consequently the superscaling function. In all steps we relate the results obtained for the scaling function to the empirical one. We establish a relationship between the single-particle widths obtained and the experimental ones.

The theoretical scheme with a detailed analysis of the various approaches considered in the evaluation of the spectral function is presented in Sec. II. Here we also show and discuss the results obtained. We present a systematic study of the scaling function as well as the momentum distribution, considering several different models and taking into account the role played by FSI. A summary of the work and our conclusions are presented in Sec. III.

II. SCALING FUNCTION IN RELATION TO THE SPECTRAL FUNCTION AND MOMENTUM DISTRIBUTION

In this section we give the main relationships used in our approach in order to find a simultaneous description of the spectral function, momentum distribution, and scaling function. As mentioned in the Introduction, the scaling function is given as a ratio between the inclusive electron-nucleus cross section and the electron-nucleon cross section at $p=|y|$ and $\mathcal{E}=0$. Within PWIA, the scaling function is expressed in terms of the spectral function by Eq. (3). It was shown in Ref. [24] that in this scheme the equations that relate the scaling function $F(q,y)$ with the spectral function in the regions of negative and positive values of the scaling variable y have the form:

$$\frac{1}{2\pi}F(q,y) = \int_{-y}^{Y(q,y)} p\, dp \int_0^{\mathcal{E}^-(p;q,y)} d\mathcal{E} S(p,\mathcal{E}), \quad \text{if } y<0, \tag{6}$$

$$\frac{1}{2\pi}F(q,y) = \int_0^{y} p\, dp \int_{\mathcal{E}^+(p;q,y)}^{\mathcal{E}^-(p;q,y)} d\mathcal{E} S(p,\mathcal{E}) + \int_y^{Y(q,y)} p\, dp \times \int_0^{\mathcal{E}^-(p;q,y)} d\mathcal{E} S(p,\mathcal{E}), \text{ if } y>0\,. \tag{7}$$

In Eqs. (6) and (7):

$$y(q,\omega) = \left\{(M_A^0+\omega)\sqrt{\Lambda^2 - M_B^{0^2}W^2} - q\Lambda\right\}/W^2, \quad (8)$$

$$Y(q,\omega) = \left\{(M_A^0+\omega)\sqrt{\Lambda^2 - M_B^{0^2}W^2} + q\Lambda\right\}/W^2, \quad (9)$$

$$\mathcal{E}^{\pm}(p;q,\omega) = (M_A^0+\omega) - \left[\sqrt{(q\pm p)^2+m_N^2} + \sqrt{M_B^{0^2}+p^2}\right], \quad (10)$$

where ω is the energy transfer, M_A^0 is the target nuclear mass, m_N is the nucleon mass, M_B^0 is the ground-state mass of the residual nucleus and $\Lambda \equiv (M_B^{0^2} - m_N^2 + W^2)/2$ with $W \equiv \sqrt{(M_A^0+\omega)^2 - q^2}$ being the final-state invariant mass.

In the RFG model the dimensionless scaling variable ψ is introduced [15–18] in the form:

$$\psi = \frac{1}{\sqrt{\xi_F}} \frac{\lambda - \tau}{\sqrt{(1+\lambda)\tau + \kappa\sqrt{\tau(1+\tau)}}}, \quad (11)$$

where $\eta_F = k_F/m_N$, $\xi_F = \sqrt{1+\eta_F^2} - 1$ is the dimensionless Fermi kinetic energy, $\kappa = q/(2m_N)$, $\lambda = \omega/(2m_N)$, and $\tau = |Q^2|/(4m_N^2) = \kappa^2 - \lambda^2$ is the dimensionless absolute value of the squared four-momentum transfer. The physical meaning of ψ^2 is the smallest kinetic energy (in units of the Fermi energy) that one of the nucleons responding to an external probe can have.

The scaling variables y and ψ are closely related [17,18]:

$$\psi = \left(\frac{y}{k_F}\right)\left[1 + \sqrt{1+\frac{m_N^2}{q^2}}\frac{1}{2}\eta_F\left(\frac{y}{k_F}\right) + \mathcal{O}\left[\eta_F^2\right]\right] \simeq \frac{y}{k_F}, \quad (12)$$

where η_F is small, typically $\approx$1/4. The dimensionless scaling function $f(\psi)$ is introduced [18] in the RFG model:

$$f_{\rm RFG}(\psi) = k_F F_{\rm RFG}(\psi) = \tfrac{3}{4}(1-\psi^2)\Theta(1-\psi^2). \quad (13)$$

As observed, the RFG model leads to a universal scaling function $f_{\rm RFG}$, which depends only on the scaling variable ψ but does not depend on the momentum transferred or on the nuclear species; that is, it superscales.

A. Theoretical spectral functions: Independent particle shell model and beyond

As noted in the Introduction, the aim of the present work is to construct a realistic spectral function that leads to good agreement with the scaling function obtained from the inclusive electron-nucleus scattering data. We start with a given form for the spectral function, viz. that of the IPSM:

$$S_{\rm IPSM}(p,\mathcal{E}) = \sum_i 2(2j_i+1)n_i(p)\delta(\mathcal{E}-\mathcal{E}_i), \quad (14)$$

where $n_i(p)$ is the momentum distribution of the shell-model single-particle state i and $\mathcal{E}_i$ is the eigenvalue of the energy of the state i. One may reasonably expect that when effects beyond mean field are considered, the dependence on the energy here would be better represented by a function with a finite width in energy instead of by a δ function. To explore the possible effect of a finite energy spread in Eq. (14), in what follows the energy dependence in Eq. (14) (the δ function) is usually replaced by a Gaussian distribution $G_{\sigma_i}(\mathcal{E}-\mathcal{E}_i)$:

$$S(p,\mathcal{E}) = \sum_i 2(2j_i+1)n_i(p)G_{\sigma_i}(\mathcal{E}-\mathcal{E}_i), \quad (15)$$

where

$$G_{\sigma_i}(\mathcal{E}-\mathcal{E}_i) = \frac{1}{\sigma_i\sqrt{\pi}} e^{-\frac{(\mathcal{E}-\mathcal{E}_i)^2}{\sigma_i^2}}, \quad (16)$$

and σ_i is a parameter for a given single-particle state i that is related to the width of the hole state i. In the present work, we focus on the case of ^{16}O, together with a few results for ^{12}C. For both nuclei we consider two parameters, σ_{1s} and σ_{1p}, that are related to the widths of the $1s$ and $1p$ hole states, respectively. We note that for simplicity we do not consider the differences in the spin-orbit partners $1p_{3/2}$ and $1p_{1/2}$ states. We look for a best fit of the parameters in order to provide a good simultaneous description of the experimental scaling function $f(\psi)$, the experimental values for the widths of the hole states, and the high-momentum tail of the momentum distribution.

With a methodical purpose in mind, we also consider and use for a comparison with the Gaussian in Eq. (16) another form of the energy dependence, the so-called Lorentzian function $L_{\Gamma_i}(\mathcal{E}-\mathcal{E}_i)$:

$$L_{\Gamma_i}(\mathcal{E}-\mathcal{E}_i) = \frac{1}{\pi}\frac{\Gamma_i/2}{(E-E_i)^2 + (\Gamma_i/2)^2}, \quad (17)$$

where Γ_i is the width for a given single-particle hole state i.

We start by taking $n_i(p)$ to be the momentum distribution of the harmonic-oscillator shell-model single-particle state i. Next, as can be seen from Eqs. (15) and (16), we account for the effects of nucleon correlations that give widths to the energy distributions of the hole strengths seen in (e,e') or $(e,e'p)$ reactions. These widths may not, in fact, be symmetric, although in the present work, for simplicity, we limit ourselves to symmetric ones. In Fig. 1 are the results for the scaling function compared with the longitudinal experimental data. There we have assumed equal values of σ_{1s} and σ_{1p} ($\sigma_{1s} = \sigma_{1p} \equiv \sigma$) and vary σ in the region $\sigma = 10$–90 MeV. In contrast, results in Figs. 2 and Fig. 3 correspond to fixed values of σ_{1s} [Γ_{1s} in the case of Lorentzian functions, see Eq. (17)] and σ_{1p} (Γ_{1p}) taken only at the extreme values 10 and 90 MeV, and vice versa.

One can see that at fixed values of the parameter σ_{1s} (Γ_{1s}) and for running values of $\sigma_{1p} = 10$ MeV ($\Gamma_{1p} = 10$ MeV) and 90 MeV, the main effects in the scaling function are observed in the shape of the curve and its maximum value, which increases significantly as σ_{1p} (Γ_{1p}) goes down. Likewise, the curve is extended in the negative ψ region. On the other hand, in the case of fixed values of σ_{1p} (Γ_{1p}) and running values of $\sigma_{1s} =$ 10 MeV ($\Gamma_{1s} = 10$ MeV) and 90 MeV, a smaller decrease of the maximum is observed and the discrepancies in the extended tail at $\psi < 0$ tend to disappear, giving rise to a similar shape for all σ_{1s} (Γ_{1s}) values considered.

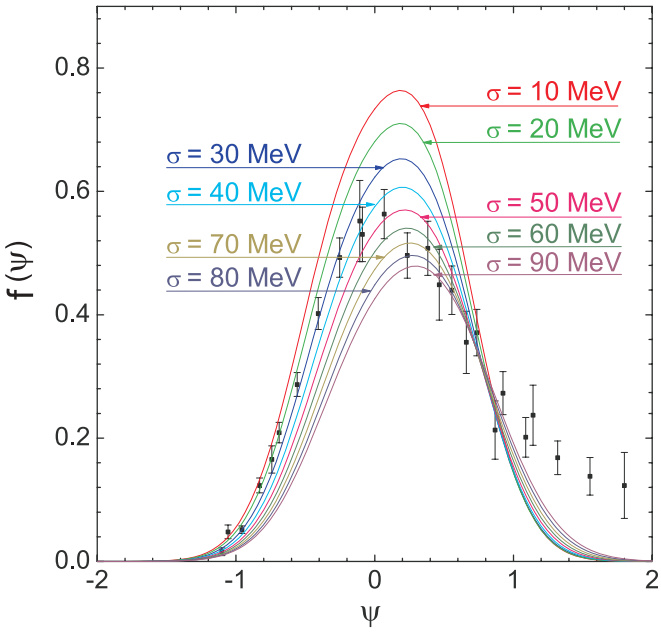

FIG. 1. (Color online) Results for the scaling function $f(\psi)$ for ^{16}O obtained using HO single-particle wave functions (for $\sigma = 10$–90 MeV) are compared with the longitudinal experimental data. The value of q is fixed to $q = 1$ GeV/c.

The main conclusion from our results presented in Figs. 1–3 is that, at least with a symmetric energy spread for the single-particle energy levels, it is not possible to get an asymmetry of the longitudinal scaling function similar to that shown by the data.

Making use of Eq. (4), we calculate the IPSM momentum distribution, which, as we are using HO single-particle wave functions, does not present a high-momentum tail. Our next step is to use natural orbitals (NOs) for the single-particle wave functions and occupation numbers employing a method where short-range *NN* correlations are taken into account. In what follows we use the NO representation of the one-body density matrix (OBDM) obtained within the lowest-order approximation of the Jastrow correlation method [29].

The NOs $\varphi_\alpha(r)$ are defined [30] as the complete orthonormal set of single-particle wave functions that diagonalize the OBDM:

$$\rho(\mathbf{r}, \mathbf{r}') = \sum_a N_a \varphi_a^*(\mathbf{r}) \varphi_a(\mathbf{r}'), \tag{18}$$

where the eigenvalues N_α ($0 \leqq N_\alpha \leqq 1$, $\sum_\alpha N_\alpha = A$) are the natural occupation numbers.

The NO single-particle wave functions are used to obtain the momentum distributions $n_i(p)$ and from them the spectral function according to Eq. (15). The results for the scaling function obtained using NOs and HO single-particle wave functions for various values of the parameters σ_{1s} and σ_{1p} are given in Fig. 4. They are represented by solid (HO) and dashed (NO) lines and compared with the RFG result (dotted), presented for reference. As observed, the main effect introduced by the use of NO, compared with HO, is an enhancement in the maximum of the order of ∼10%. In contrast, the tail is slightly reduced in the region of negative ψ. However, notice that both models lead to a weak asymmetry in the scaling function $f(\psi)$ that is not in accordance with the significant tail extended to positive ψ-values, seen in the analysis of (e, e') data. It should be mentioned here that in addition to $1s$ and $1p$ components there are also $1d$ and $1f$ components in the NOs obtained from the Jastrow correlation method. Unless specified otherwise, we take the same values of σ for all of them.

In Fig. 5 we present the evolution of the scaling function $f(\psi)$ for different values of q, from 100 to 2000 MeV/c. Results have been obtained making use of the HO momentum distributions for the $1p$ and $1s$ shells in ^{16}O. From these, one gets the spectral function according to Eqs. (15) and (16) and finally the scaling function using the expressions in Eqs. (6) and (7). As already mentioned, the HO model is not capable of producing the strong asymmetry observed in the data, but it can be seen that for $q > 600$–700 MeV/c, scaling of the first kind is fulfilled.

In what follows, we focus on the study of the momentum distribution obtained in different approaches. Results are presented in Fig. 6, where we use a log scale in order to

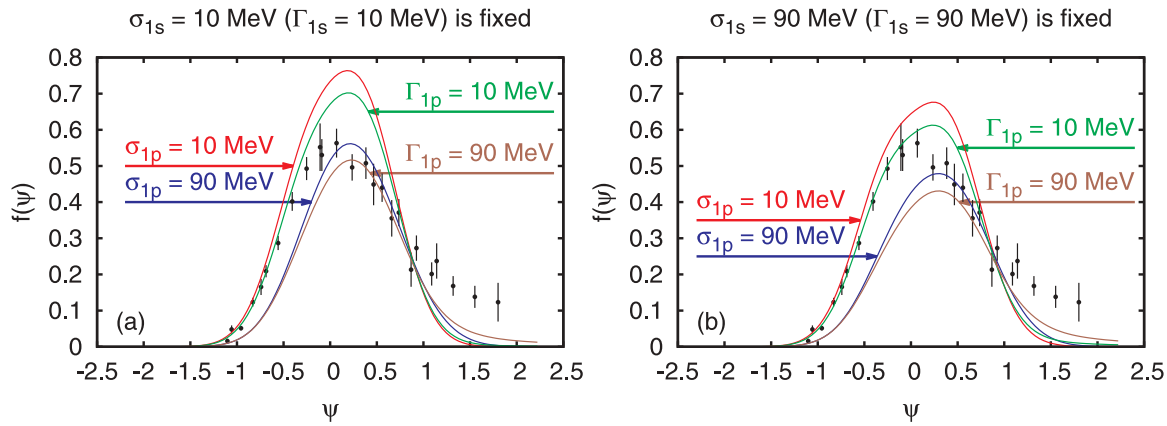

FIG. 2. (Color online) Results for the scaling function $f(\psi)$ for ^{16}O obtained using HO single-particle wave functions. The values of σ_{1s} [Γ_{1s} in the case of Lorentzian functions, see Eq. (17)] are fixed and $\sigma_{1p} = 10$ MeV ($\Gamma_{1p} = 10$ MeV) and $\sigma_{1p} = 90$ MeV ($\Gamma_{1p} = 90$ MeV) have been used. The results are compared with the longitudinal experimental data. The value of q is fixed to $q = 1$ GeV/c.

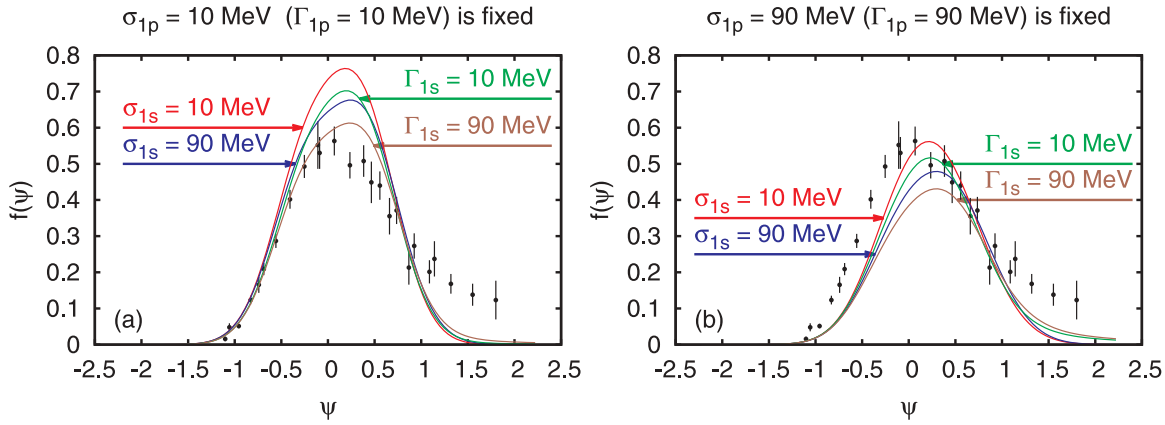

FIG. 3. (Color online) Results for the scaling function $f(\psi)$ for ^{16}O obtained using HO single-particle wave functions. The values of σ_{1p} (Γ_{1p}) are fixed and $\sigma_{1s} = 10$ MeV ($\Gamma_{1s} = 10$ MeV) and $\sigma_{1s} = 90$ MeV ($\Gamma_{1s} = 90$ MeV) have been used. The results are compared with the longitudinal experimental data. The value of q is fixed to $q = 1$ GeV/c.

emphasize the differences. The RFG momentum distribution is compared with the result obtained using HO single-particle wave functions and the NOs from the Jastrow-correlated approach [29]. The nucleon momentum distribution n^{LFD} obtained in Refs. [23,31] by using the light-front dynamics (LFD) method [32] is presented in Fig. 6 as well. We also show in the same figure the results obtained in Ref. [33] within the relativistic mean field (RMF) model with and without taking into account FSI. Finally, we give in Fig. 6 as an example (being considered and used in our previous work) the result obtained with the coherent density fluctuation model (CDFM) [4,7,11]; see also [21,23]. The model is a natural extension of the RFG model. It is based on the δ-function limit of the generator coordinate method [34] and accounts for long-range NN correlations of collective type. In it the nucleon momentum distribution has the form:

$$n(\mathbf{k}) = \int d\mathbf{r} W(\mathbf{r}, \mathbf{k}), \tag{19}$$

where the CDFM Wigner distribution function is:

$$W(\mathbf{r}, \mathbf{k}) = \int_0^\infty dx |F(x)|^2 W_x(\mathbf{r}, \mathbf{k}), \tag{20}$$

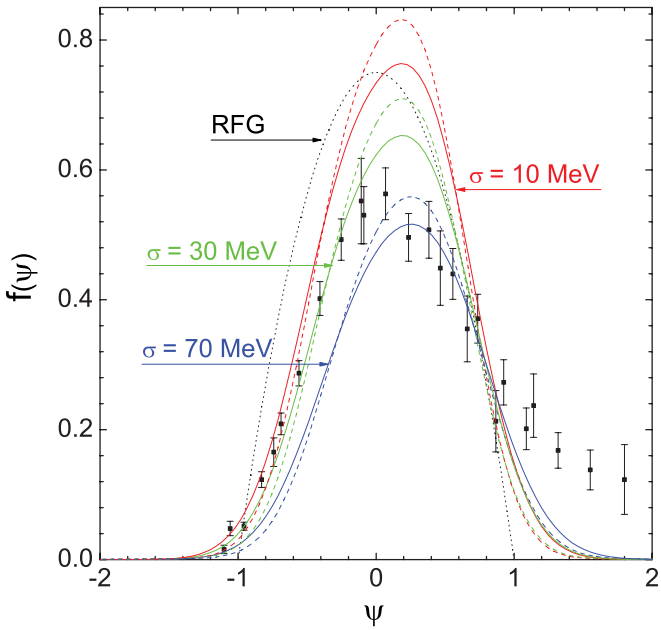

FIG. 4. (Color online) Results for the scaling function $f(\psi)$ for ^{16}O obtained using NOs (dashed lines) and harmonic oscillator (HO) single-particle wave functions (solid lines) for various values of the parameters $\sigma_{1s} = \sigma_{1p} = 10$ MeV (red lines), 30 MeV (green lines), and 70 MeV (black lines). The RFG results are shown for comparison (dotted line). The value of q is fixed to $q = 1$ GeV/c.

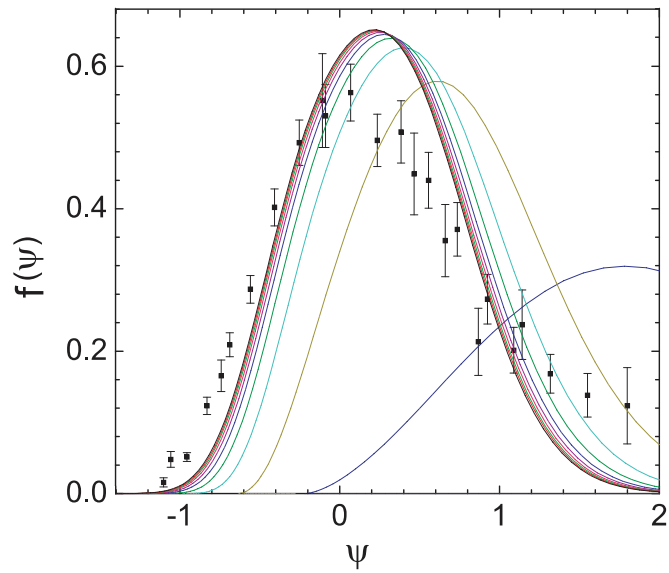

FIG. 5. (Color online) The scaling function $f(\psi)$ for ^{16}O calculated using HO single-particle wave functions (with $\sigma = 0$), presented as a function of ψ for a range of fixed values of q extending from 100 MeV/c (right-most curve) to 2000 MeV/c (left-most curve) in steps of 200 MeV/c. For $q > 700$ MeV/c, scaling of the first kind is seen to be fulfilled.

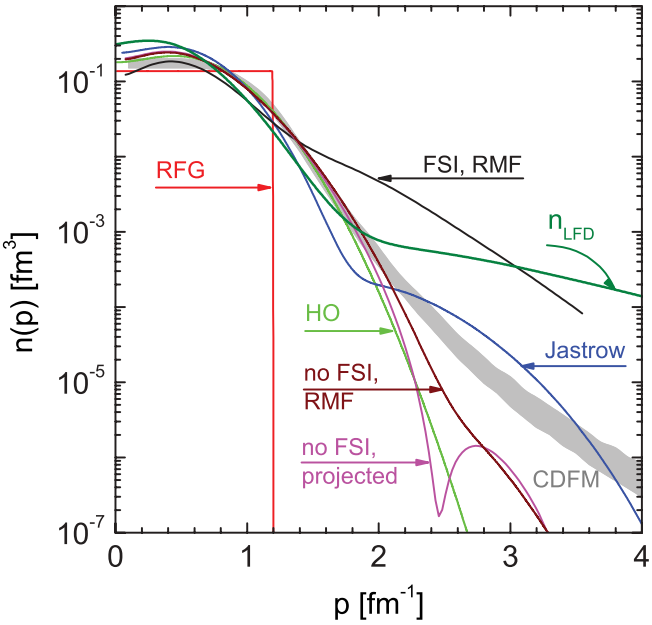

FIG. 6. (Color online) Results for the momentum distribution for ^{12}C obtained using harmonic oscillator (HO) single-particle wave functions (green line); NO taken from the Jastrow model (blue line); RFG (red line); CDFM results (gray area [21,23]); LFD results (olive line [23]). Normalization: $\int d\mathbf{k} n(\mathbf{k}) = 1$.

with

$$W_x(\mathbf{r},\mathbf{k}) = \frac{4}{(2\pi)^3}\Theta(x-|\mathbf{r}|)\Theta(k_F(x)-|\mathbf{k}|) \tag{21}$$

and

$$k_F(x) = \left[\frac{3\pi^2}{2}\rho_0(x)\right]^{1/3}, \quad \rho_0(x) = \frac{3A}{4\pi x^3}. \tag{22}$$

The model weight function $F(x)$ is obtained by means of a known density distribution $\rho(r)$ for a given nucleus:

$$|F(x)|^2 = -\frac{1}{\rho_0(x)}\left.\frac{d\rho(r)}{dr}\right|_{r=x}, \quad (\text{at } d\rho(r)/dr \leqslant 0). \tag{23}$$

The CDFM has been applied to studies of the superscaling phenomenon [20–23] in inclusive electron-nucleus scattering, as well as to analyses of neutrino and antineutrino scattering by nuclei of both charge-changing [23,35] and neutral-current [36] types.

Before entering into a discussion of the RMF results, it is interesting to point out the significant differences introduced by the other models. As noticed, the presence of nucleon correlations (through the Jastrow approach) leads to a significant tail at high momentum values compared with the pure HO result. On the contrary, the momentum distribution is slightly reduced for small-to-intermediate p. As can be seen, the tail at high p is extremely large for $n^{\mathrm{LFD}}(p)$ and is also present in the case of the CDFM model. The latter is a result of the *NN* correlation effects accounted for in the model. Later in this work we also show the role of these correlations within the CDFM approach [23] (with phenomenologically introduced FSI effects) on the scaling function $f(\psi)$ in the cases of ^{12}C and ^{16}O.

Next we discuss in more detail how the momentum distribution function is evaluated within the general framework of the RMF. The particular case where FSI are turned on is considered in the next subsection. In the RMF case without FSI, the momentum distribution $n^{\mathrm{RMF}}(p)$ is given in the form:

$$n^{\mathrm{RMF}}(p) = \sum_{\text{shells}} n_{\text{shell}}(p), \tag{24}$$

with

$$n_{\text{shell}}(p) = |\varphi_{\text{shell}}(p)|^2, \tag{25}$$

where $\varphi_{\text{shell}}(p)$ are single-particle four-component wave functions that are solutions of the Dirac equation with an RMF (relativistic Hartree) potential.

It is also interesting to consider the momentum distribution for the case in which the relativistic bound nucleon wave functions are projected over positive-energy components. In this case, the four-spinors $\varphi_{\text{shell}}(p)$ go into four-spinors $\widetilde{\varphi}_{\text{shell}}(p)$ by the action of the positive-energy projection operator

$$\widetilde{\varphi}_{\text{shell}}(p) = \left(\frac{\not{p}+m}{2m}\right)\varphi_{\text{shell}}(p). \tag{26}$$

Hence the "positive-energy projected" momentum distribution results:

$$\widetilde{n}^{\mathrm{RMF}}(p) = \sum_{\text{shells}} \widetilde{n}_{\text{shell}}(p) = \sum_{\text{shells}} |\widetilde{\varphi}_{\text{shell}}(p)|^2. \tag{27}$$

The latter from Eq. (27) is labeled in Fig. 6 as "no FSI, projected," although we should point out that it differs from the usual nonrelativistic analyses, where two-component Schrödinger-like equations are considered and a nonrelativistic reduction of the relativistic 4×4 current operator into a 2×2 form is used. Here, we project out the negative-energy components of the bound nucleon wave functions while a fully four-component description of the Dirac spinors is maintained. The outgoing nucleon is described by means of a relativistic (Dirac) plane wave. These two assumptions (i.e., plane waves in the final state and positive-energy projection in the initial one) lead to the so-called PWIA, which should be distinguished from the relativistic plane-wave impulse approximation (RPWIA), where the plane-wave approach for the ejected nucleon is also considered, but where the fully relativistic bound nucleon wave function (without projection) is used.

In PWIA, the exclusive electron $(e,e'N)$ cross section factorizes in the form:

$$\left.\frac{d\sigma}{d\Omega' d\epsilon' d\Omega_N}\right|_{\mathrm{PWIA}} = K\sigma^{eN}\widetilde{n}_{\text{shell}}(p), \tag{28}$$

where K is a kinematical factor and σ^{eN} is the electron-nucleon cross section. Thus Eq. (28) makes it possible to obtain the momentum distribution for different shells by means of the cross section calculated within the PWIA:

$$\widetilde{n}_{\text{shell}}(p) = \frac{\left[\frac{d\sigma}{d\Omega' d\epsilon' d\Omega_N}\right]_{\mathrm{PWIA}}}{K\sigma^{eN}}. \tag{29}$$

This result coincides with the one given through the positive-energy-projected wave functions in Eq. (27).

Results for $n^{\mathrm{RMF}}(p)$ (labeled as "no FSI, RMF") and $\widetilde{n}^{\mathrm{RMF}}(p)$ (no FSI, projected) are compared in Fig. 6. As shown, $\widetilde{n}^{\mathrm{RMF}}(p)$ follows the HO result closely, showing a steep slope with increasing p. Likewise, $n^{\mathrm{RMF}}(p)$ presents a similar behavior but without the diffraction minimum due to the presence of the lower components in the relativistic bound nucleon wave functions. These results confirm previous studies presented in [37].

B. The role of FSI

The factorized form of the $(e, e'N)$ cross section shown in Eq. (28) does not apply when final-state interactions are included in the description of the reaction mechanism. However, one can introduce a function given as the ratio between the differential cross section and the single-nucleon cross section (multiplied by the kinematical factor K). This is usually called the reduced cross section or distorted momentum distribution:

$$\rho(p) = n^{\mathrm{dist}}(p) = \frac{\left[\frac{d\sigma}{d\Omega' d\epsilon' d\Omega_N}\right]_{\mathrm{FSI}}}{K\sigma^{eN}}. \tag{30}$$

Although in Eq. (30) we show the function n^{dist} to be only dependent on the missing momentum p, this is not so in general because of the non-factorized form of the $(e, e'N)$ differential cross section when FSI are included. The distorted momentum distribution depends not only on the missing momentum p but also on the other independent variables in the scattering process, for example the momentum transfer q. Hence, calculations for different kinematical situations may lead to slightly different distorted momentum distributions. However, this dependence has been proven to be weak in most cases [38–40]. The resulting effective momentum distribution $n^{\mathrm{dist}}(p)$ for a momentum transfer of 1 GeV/c and the momentum of the final nucleon equal to the momentum transfer is also displayed in Fig. 6 (labeled as "FSI, RMF"). In computing this effective momentum distribution using Eq. (30), the same real scalar and vector potentials that describe the bound nucleons are employed to describe the final nucleon. The nonlinear effective interaction NLSH [41] has been used.

As observed, FSI evaluated within the RMF approach gives rise to the presence of a very significant tail at high-missing momentum, which is several orders of magnitude larger than the results obtained within the plane-wave approach. On the contrary, $n^{\mathrm{dist}}(p)$ is smaller for p values below the Fermi momentum. It is important to point out that the right amount of asymmetry in the longitudinal scaling function required by (e, e') data is also reproduced by a semirelativistic shell model when the continuum states are described with the Dirac-equation-based (DEB) equivalent potential to the RMF employed here [42,43].

Once the distorted RMF momentum distribution has been obtained [Eq. (30)], we calculate the "distorted" spectral function $S^{\mathrm{dist}}(p, \mathcal{E})$ using Eqs. (15) and (16). Finally, the corresponding scaling and superscaling functions can be evaluated making use of the procedure outlined through Eqs. (5)–(7). The results for $f(\psi)$ are given for different values of $\sigma = \sigma_{1s} = \sigma_{1p}$ (from 10 to 100 MeV) in Fig. 7. Also, for completeness, we show in Fig. 7 the scaling function $f(\psi)$ obtained within the RMF+FSI model, but evaluated directly from the inclusive (e, e') differential cross section [33], that is,

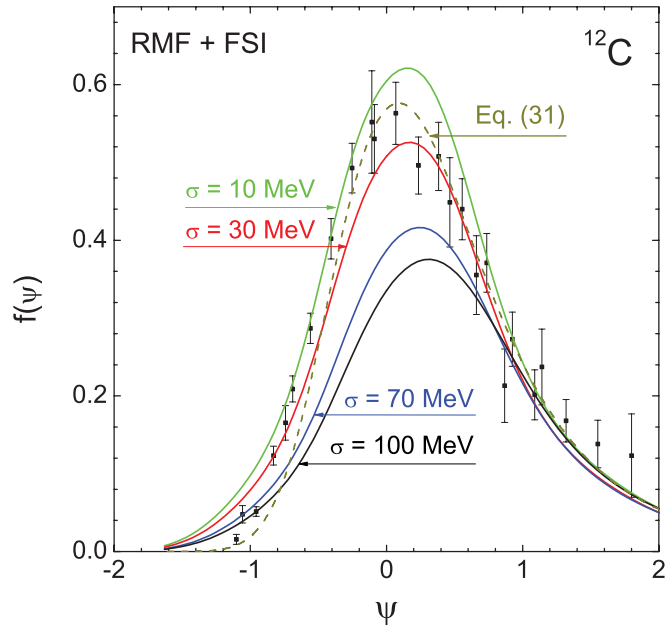

FIG. 7. (Color online) Results for the scaling function $f(\psi)$ obtained using single-particle wave functions taken from RMF + FSI for calculation of $n_i(p)$ and for various values of the parameters $\sigma = \sigma_{1s} = \sigma_{1p}$. Also shown are results obtained through Eq. (31). Momentum transfer fixed to $q = 1$ GeV/c.

$$f^{\mathrm{dist}}(\psi) = k_F \frac{\left[\frac{d\sigma}{d\epsilon' d\Omega'}\right]^{RMF+FSI}_{(e,e')}}{\overline{\sigma}^{eN}(q, \omega; p = |y|, \mathcal{E} = 0)}. \tag{31}$$

Results in Fig. 7 show that the RMF with FSI included gives rise to an asymmetrical scaling function, which follows the behavior of data, irrespective of whether we use Eqs. (15) and (30) or we use Eq. (31). In the first case, significant discrepancies emerge when different values of the σ parameter are used in the Gaussian energy-dependent functions. The scaling function obtained from Eq. (31) is close to that obtained from Eqs. (15) and (30) for $\sigma = 30$ MeV. We note that for the negative ψ region, the scaling function obtained from the RMF calculation for the cross section lies well below the data. The comparison with data in this region is thus improved when a finite width for the energy is introduced in the spectral function. As observed, the case $\sigma = 30$ MeV is the one that agrees better with experiment and with the theoretical curve obtained directly from the inclusive cross section [see Eq. (31)]. We use $\sigma = \sigma_{1s} = \sigma_{1p}$ to check the dependence of the scaling function $f(\psi)$ on σ. Below we discuss the optimal values of these parameters $\sigma_{1s} \neq \sigma_{1p}$, and check the results for the scaling functions when these parameters give widths close to the experimental ones.

In addition to the description of FSI within the framework of the RMF model, we have also considered alternative analyses of final-state interactions in the case of inclusive electron-nuclei processes. In what follows, we discuss a method proposed in Ref. [44] and present the results we obtained with this method.

According to the authors of Ref. [44], two types of FSI effects, Pauli blocking and the interaction of the struck nucleon with the spectator system described by means of the time-independent optical potential (OP),

$$U = V - \imath W, \tag{32}$$

proposed in Ref. [45], can be accounted for by replacing in the PWIA expression for the inclusive electron-nucleus cross section

$$\frac{d\sigma_t}{d\omega d|\mathbf{q}|} = 2\pi\alpha^2 \frac{|\mathbf{q}|}{E_{\mathbf{k}}^2} \int dE\, d^3p\, \frac{S_t(\mathbf{p}, E)}{E_{\mathbf{p}} E_{\mathbf{p}'}} \delta \times (\omega + M - E - E_{\mathbf{p}'}) L_{\mu\nu}^{em} H_{em,t}^{\mu\nu}, \tag{33}$$

the energy-conserving δ function by

$$\delta(\omega + M - E - E_{\mathbf{p}'}) \to \frac{W/\pi}{W^2 + [\omega + M - E - E_{\mathbf{p}'} - V]^2}. \tag{34}$$

In Eq. (33), the index t denotes the nucleon isospin, $L_{\mu\nu}^{\rm em}$ is the leptonic tensor, $H_{\rm em,t}^{\mu\nu}$ is the hadronic tensor, and $S_t(p, E)$ is the proton (neutron) spectral function. The terms $E_{\mathbf{k}}$, $E_{\mathbf{p}}$, $E_{\mathbf{p}'}$, and E represent the initial electron energy, the energy of the nucleon inside the nucleus, the ejected nucleon energy, and the removal energy, respectively (see Ref. [44] for details).

The real and imaginary parts of the OP in Eqs. (32) and (34) are obtained from the Dirac OP in Ref. [46]. We use spatially averaged values, evaluating them at the r values that match their respective root mean-squared radii [46]. As a result the OP $U(p')$ related to the scalar (S) and vector (V) part of the potential in Ref. [46] is obtained in the form (see also Ref. [44]):

$$E_{\mathbf{p}'} + U(\mathbf{p}') = \sqrt{[M + S(T_{\mathbf{p}'}, \bar{r}_S)]^2 + \mathbf{p}'^2} + V(T_{\mathbf{p}'}, \bar{r}_V). \tag{35}$$

We consider also an OP with the imaginary part of the potential $U(p')$ given in [47]:

$$W = \frac{\hbar c}{2} \rho_{\rm nucl} \sigma_{NN} \frac{|\mathbf{p}'|}{E_{\mathbf{p}'}}, \tag{36}$$

where the values of $\rho_{\rm nucl}$ and σ_{NN} for ^{16}O are taken to be: $\rho_{\rm nucl} = 0.16$ fm^{-3} and $\sigma_{NN} = 40$ mb.

In Fig. 8 we give the calculated real and imaginary parts of the OP $U(p')$ from Eq. (35) and the imaginary part of the OP from Eq. (36). As noted in [44], for $|\mathbf{p}'| > 580$ MeV/c, the real part of $U(\mathbf{p}')$ is positive, which is inconsistent with correlated Glauber theory [48]. Therefore, following Ref. [44] when $|\mathbf{p}'| > 580$ MeV/c, the real part of the OP is set to zero. As was noted in Ref. [48], the real and the imaginary part of the optical potential quantitatively have very different effects and describe different aspects of the FSI. The imaginary part (W) accounts for two-body scattering processes involving large momentum transfers, which lead to a strong damping of the motion of the recoiling particle, whereas the real part (U) produces a shift of its energy. The effect of the imaginary part is known to be dominant at large momentum.

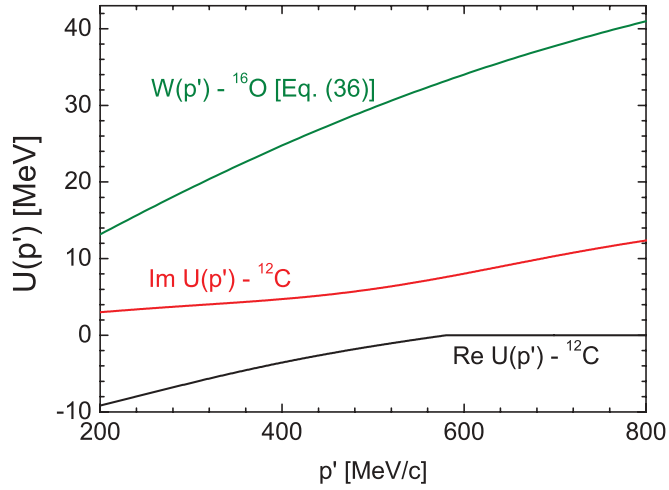

FIG. 8. (Color online) The real and imaginary parts of the optical potential $U(p')$ for ^{12}C calculated by Eq. (35) using a Dirac OP from [46] and the imaginary part of the optical potential for ^{16}O given by Eq. (36).

Following the approach of Ref. [44], we calculate the scaling function according to Eq. (2), but evaluating the cross section in the numerator by accounting for FSI using the Dirac OP; i.e., exchanging the δ function in Eq. (33) as shown in Eq. (34). The expression for $S(p, \mathcal{E})$ in Eq. (33) is taken in the form in Eq. (15), where we use momentum distributions $n_i(p)$ obtained in different approaches. The results in the case of the RFG model spectral function are presented in Fig. 9 for a given momentum transfer $q = 1$ GeV/c and energy of the initial electron $\epsilon = 1$ GeV with and without accounting for FSI. The scaling function $f(\psi)$ using the $S_{\rm IPSM}(p, \mathcal{E})$ of Eq. (14) with HO single-particle wave functions is presented in Fig. 10 for $q = 1$ GeV/c and $\epsilon = 1$ GeV. In this case, we consider two different types of the time-independent optical potential for ^{16}O: (i) the one obtained by Eqs. (32),(34), and (35) using the scalar and vector part of the potential from [46] and (ii) using the imaginary part of the potential $U(\mathbf{p}')$ from Eq. (36) [47].

As can be seen from Figs. 9 and 10, FSI lead to a decrease in the maximum of the scaling function, while an enhancement of the tails is observed for both negative and positive values of ψ. The importance of the type of time-independent optical potential used is shown in Fig. 10.

In Figs. 9 and 10, as well as in Fig. 11, we give for a comparison the results for the scaling function obtained within the CDFM approach [23] in which FSI effects are introduced phenomenologically. As can be seen, accounting for FSI together with the effects of *NN* correlations is necessary for a reasonable explanation of the experimental data for the longitudinal scaling function, especially the maximum and the tail of $f(\psi)$ at $\psi > 1$.

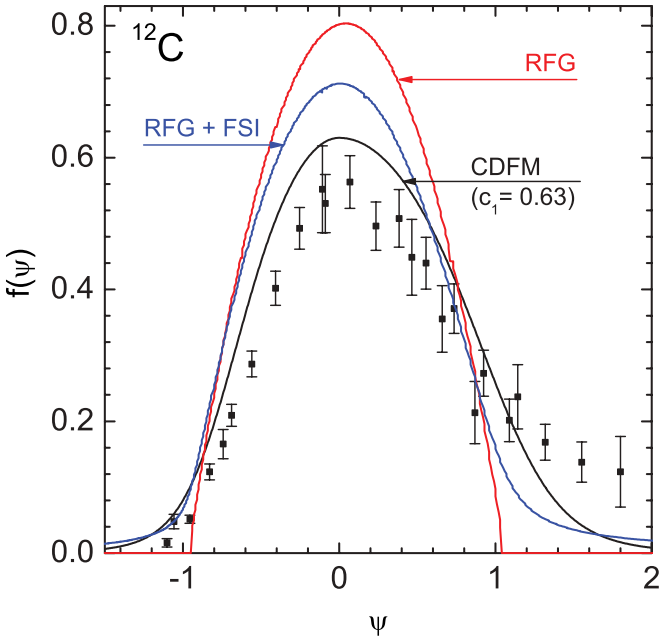

FIG. 9. (Color online) Results for the scaling function $f(\psi)$ with and without taking into account FSI in the RFG model (for a given momentum transfer $q = 1$ GeV/c and energy of the initial electron $\epsilon = 1$ GeV) are compared with the longitudinal experimental data and CDFM results using $c_1 = 0.63$ [23].

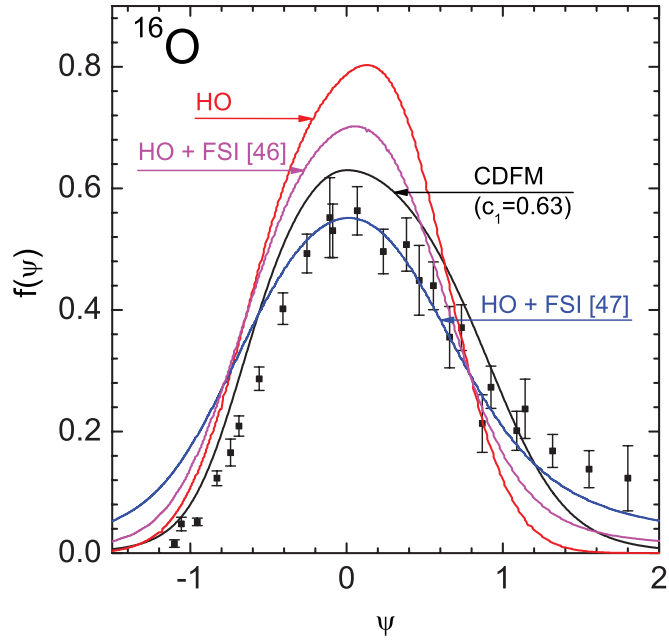

FIG. 10. (Color online) Results for the scaling function $f(\psi)$ with and without taking into account FSI using the spectral function in the IPSM [Eq. (14)] with HO single-particle wave functions (for a given momentum transfer $q = 1$ GeV/c and energy of the initial electron $\epsilon = 1$ GeV), compared with the longitudinal experimental data and CDFM results using $c_1 = 0.63$ [23].

Finally, we consider results that correspond to a spectral function constructed with NOs from the Jastrow correlation method, within this alternative way to take into account FSI. These results are presented in Fig. 11 for $q = 1$ GeV/c and electron beam energy $\epsilon = 1$ GeV. (We consider two different time-independent optical potentials for ^{16}O, the same as in Fig. 10.) The value of the parameter σ_{1s} is fixed to be 8.7 MeV (that corresponds to the experimental width of the $1s$ state in ^{16}O taken from Ref. [49]) and $\sigma_{1p} = \sigma_{1d} = \sigma_{1f} = 0.5$ MeV. The results depend very weakly on the choice of parameters σ_i.

The next step of our work was to obtain optimal values of the parameters σ_i in the Gaussians $G_{\sigma_i}(\mathcal{E} - \mathcal{E}_i)$ [Eq. (16)] by an additional fitting procedure. These values of σ_i are compared with the experimental widths of the hole states. The results of our calculations in the case of the RMF model accounting for the FSI are given in Fig. 12. Here the value of the parameter σ_{1s} is fixed to be 7.8 MeV (that corresponds to the experimental width of the $1s$ state in ^{12}C taken from [49]), and the values of σ_{1p} are varied. Figure 12 also shows the result for the scaling function obtained when more recent experimental data for the full width at half maximum (FWHM) for $1s$ and $1p$ states (taken from [50]) are used. Notice that the latter result (black dotted line) almost coincides with the case of $\sigma_{1p} = 5$ MeV and $\sigma_{1s} = 7.8$ MeV. As can be seen, the results for the scaling function cannot reproduce very well the experimental data using experimental widths.

Finally, in Fig. 13, the results for the scaling function $f(\psi)$ calculated using single-particle functions taken from HO and RMF+FSI and for two energy-dependence functions, Lorentzian and Gaussian, are presented and compared. We note the good agreement of $f(\psi)$ (using widths close to the experimental $\Gamma_{1p} = 6$ MeV, $\Gamma_{1s} = 20$ MeV and single-particle functions taken from RMF+FSI), including the maximum value and the asymmetry of the scaling function. In this way, together with the results for the momentum distribution and the scaling function, we obtain a completion and self-consistency of our study.

III. CONCLUSIONS

Analysis of world (e, e') data has clearly demonstrated the validity of scaling arguments. Not only has the scaling phenomenon been proven to be fulfilled, but also the specific shape of the scaling function, with a significant tail extending to high values of the scaling variable, has emerged from the separated (e, e') longitudinal data. These results constitute a strong constraint for any theoretical model describing electron scattering reactions. Moreover, the scaling function is an observable that has been used in the past in order to get information on the spectral function $S(p, \mathcal{E})$ and/or the nucleon momentum distributions of nucleons in nuclei $n(p)$. However, as explored in detail in our previous work [24], the connection between the scaling function [given directly from the analysis of (e, e') data] and $S(p, \mathcal{E})$ or $n(p)$ only exists under very restrictive conditions: (i) the PWIA in the description of the reaction mechanism, and (ii) additional assumptions on the integration limits consistent with the kinematically allowed region. Being aware of these restrictions and with some caution in the discussion of results, the link of the spectral function/momentum distribution with scattering observables

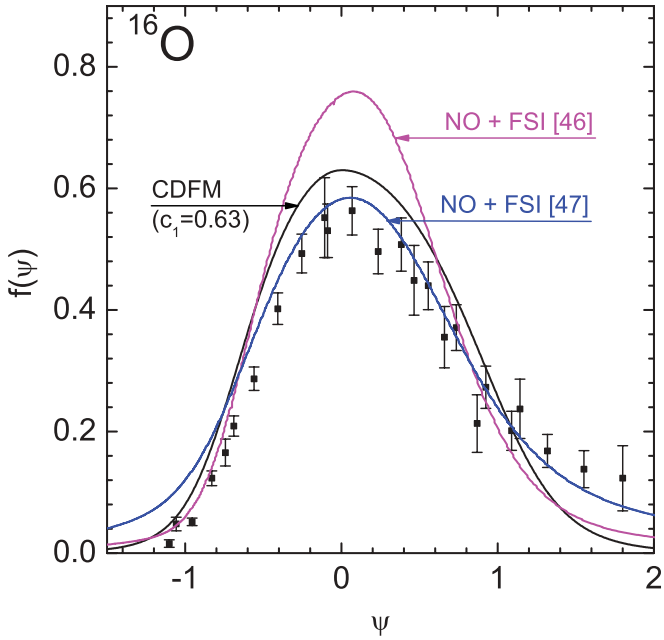

FIG. 11. (Color online) Results for the scaling function $f(\psi)$ taking into account FSI using NOs from the Jastrow correlation method (for a given momentum transfer $q = 1$ GeV/c, energy of the initial electron $\epsilon = 1$ GeV, and parameters $\sigma_{1s} = 8.7$ MeV, $\sigma_{1p} = \sigma_{1d} = \sigma_{1f} = 0.5$ MeV), compared with the longitudinal experimental data and CDFM results using $c_1 = 0.63$ [23].

remains a delicate issue in nuclear physics. Effects beyond the PWIA, such as FSI, meson-exchange currents, rescattering processes, etc., which may have very important roles to play in describing (e, e') processes, should be incorporated in the general analysis.

In this paper, we extend the previous work presented in Ref. [24] by considering several models dealing with the nuclear structure and including as well different descriptions to account for FSI. From the momentum distributions provided by three nuclear models — harmonic oscillator, natural orbitals with Jastrow-type correlations, and relativistic mean field — we construct the spectral functions where the energy dependence given through the δ function has been changed by introducing Gaussian distributions. In this way, we present a systematic analysis for different values of the Gaussian distribution parameters related to the width of the hole states. Finally, the scaling function is evaluated by making use of the general derivative expressions that connect it with the spectral function. We have explored in detail the role played by Gaussian or Lorentzian energy dependencies in the scaling function showing that, although significant differences may emerge, all models based on PWIA lead to scaling functions, which do not show the asymmetry that data exhibit, with an extended tail at high positive values of the scaling variable ψ. At the same time, we note that the width in energy introduced for the hole state, as opposed to the δ function of the strict IPSM, can, however, improve the agreement with data in the negative ψ region of the scaling function.

Effects of FSI have been proven to be essential in the description of electron scattering reactions. Hence, we have included FSI in our analysis within the framework of the RMF and the method using a complex optical potential [44]. In the former, we obtain the reduced cross section (or effective distorted momentum distribution) for each shell as the ratio between the exclusive $(e, e'N)$ cross section evaluated within the RMF model, and FSI included, and the corresponding single-nucleon cross section. These "momentum distributions" incorporate the role of FSI, and they can be used to get the spectral function following the same procedure as in the previous case (PWIA). Again, we perform a systematic analysis by considering different values of Gaussian and Lorentzian widths. Finally, the scaling function is directly evaluated from the spectral function. We have compared these results with the one obtained directly from the ratio between the inclusive (e, e') cross section (evaluated within the RMF+FSI model) and the single-nucleon cross section taken at $p = |y|$ and $\mathcal{E} = 0$. In all cases, the results obtained clearly show the essential role of FSI in producing the required asymmetry in the scaling function, i.e., to be consistent with data. Concerning the second method we explored for including FSI following Ref. [44], we note that its usage leads only to qualitative description of the experimentally observed asymmetry of the scaling function. As can be seen from Figs. 9–11, the asymmetry due to the higher tail of $f(\psi)$ for positive values of ψ is not very different for the three cases considered: the RFG model, the case with HO single-particle wave functions, and that with natural orbitals. In addition, the obtained asymmetry is rather similar in the

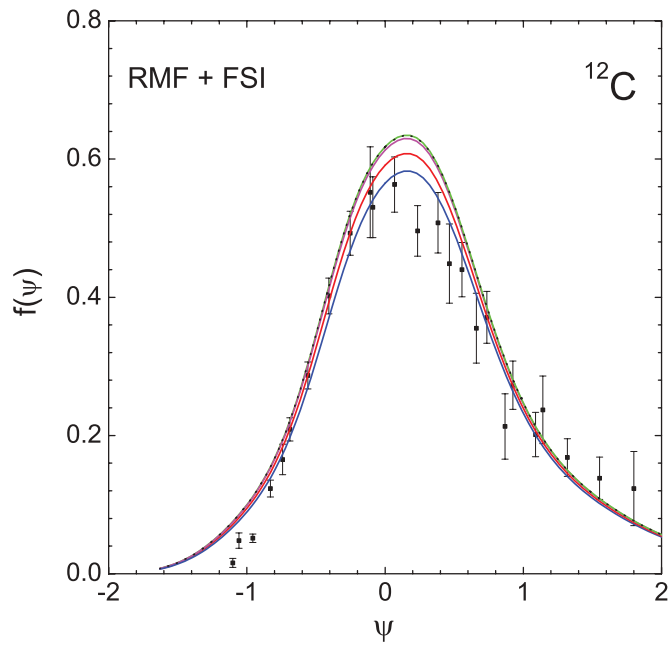

FIG. 12. (Color online) Results for the scaling function $f(\psi)$ obtained using single-particle wave functions taken from RMF + FSI for calculation of $n_i(p)$. Five curves are shown. Four (given by solid lines) correspond to $\sigma_{1s} = 7.8$ MeV taken from [49] and σ_{1p} ranging from 5 MeV (green line) to 20 MeV (blue line) in steps of 5 MeV. The fifth curve (black dotted line) corresponds to widths for $1s$ and $1p$ states taken from [50] (FWHM$_{1s} = 20$ MeV and FWHM$_{1p} = 6$ MeV). Momentum transfer: $q = 1$ GeV/c.

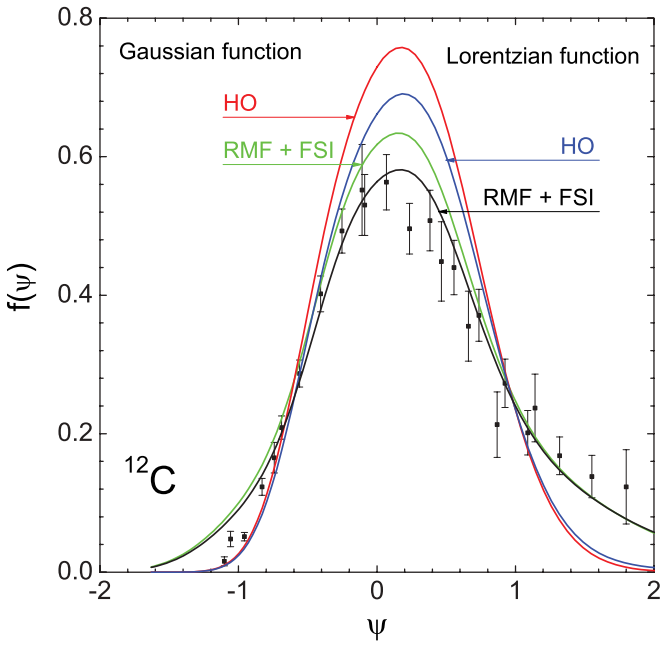

FIG. 13. (Color online) Results for the scaling function $f(\psi)$ obtained using single-particle wave functions taken from RMF+FSI for calculation of $n_i(p)$ (parameters $\Gamma_{1p} = 6$ MeV, $\Gamma_{1s} = 20$ MeV are fixed to the experimental widths of the $1p$ and $1s$ states in ^{12}C [50]) and two energy dependence functions, Lorentzian and Gaussian.

cases when nonrelativistic or relativistic optical potentials are used to account for the FSI. Here we would like to emphasize that considerably larger asymmetry is obtained in the RMF+FSI method (see Figs. 12 and 13), especially when experimental widths with the Lorentzian function are used in the calculations (see Fig. 13). So, in the case of the RMF+FSI method, the values of $f(\psi)$ for positive values of ψ describe the experimental data quite satisfactorily.

To summarize, our extensive study with different nuclear models based on the independent particle shell model and even incorporating short-range nucleon correlations through the use of NOs within the Jastrow method, show different results for the momentum distributions, particularly at high-missing momenta, where nucleon correlations give rise to the presence of an important tail. However, the scaling functions obtained from them do not present the strong asymmetry at positive ψ as given by the analysis of data. We have proven that such a "strong" asymmetry in $f(\psi)$ does not emerge even when a broader energy dependence is assumed in the spectral function, but it does emerge when FSI are taken into account. In particular, taking into account final-state interactions in the RMF approach produces, in addition to a strong tail at high p in the nucleon momentum distribution, a scaling function with the right amount of asymmetry in accordance with data.

From the results obtained in the present work, we have established and considered the relationship between the longitudinal scaling function $f(\psi)$ and the spectral function $S(p, \mathcal{E})$, accounting for the restrictive condition of the PWIA in the description of the reaction mechanism and, correspondingly, with the momentum distribution at the specific conditions for the kinematically allowed region (the excitation energy $\mathcal{E}_{\max} \to \infty$). We studied the ingredients of the spectral function, namely the single-particle momentum distributions $n_i(p)$ and the hole-state energy distributions. In several consequent steps (starting with the IPSM) with increasing complexity beyond the MFA, we showed that the $n_i(p)$ have to be considered within models in which the nucleon correlations are taken into account. This leads to the existence of high-momentum components of the momentum distributions. The methodical study of the energy distribution of the hole states showed that distributions with broader energy dependence (due to the residual interaction) have to be considered, with single-particle widths that are close to the empirically observed ones. The energy distributions must have more complicated form than the Gaussian one, e.g., the Lorentzian one. However, it was pointed out that all mentioned conditions are clearly necessary but are not sufficient for a successful description of the experimentally observed asymmetry of the scaling function $f(\psi)$; specifically, they give a weaker asymmetry at positive values of ψ. We pointed out that this characteristic feature of $f(\psi)$ can be reached only if the FSI (and other peculiarities of the electron scattering beyond the PWIA) are carefully taken into account. This was reached in the case of RMF+FSI, while other methods using complex optical potentials for FSI lead to results that have some discrepancies with the experimental longitudinal scaling function $f(\psi)$ (e.g., for $\psi < -0.9$ and $\psi > 1.2$), and they must be used with caution. The obtained results open a new perspective on the extraction of information on momentum distribution from experimental inclusive (e, e') data.

ACKNOWLEDGMENTS

This work was partially supported by DGI (MICINN-Spain) contracts no. FIS2008-01301, FIS2008-04189, PCI2006-A7-0548, FPA2007-62216, and FPA2010-17142; the Spanish Consolider-Ingenio programme CPAN (CSD2007-00042); the Junta de Andalucía; and the INFN-MICINN collaboration agreements no. FPA2008-03770-E and ACI2009-1053, "Study of relativistic dynamics in neutrino and electron scattering," as well as the Bulgarian National Science Fund under contracts no. DO-02-285 and DID–02/16–17.12.2009 and by Universidad Complutense de Madrid (Grupos UCM, 910059). One of the authors (M.V.I.) is grateful for the warm hospitality given by the Universidad Complutense de Madrid (UCM) and for support during his stay there from the State Secretariat of Education and Universities of Spain (N/Ref. SB2009-0007). This work is also supported in part (T.W.D.) by the US Department of Energy under cooperative agreement no. DE-FC02-94ER40818.

[1] D. B. Day, J. S. McCarthy, T. W. Donnelly, and I. Sick, Ann. Rev. Nucl. Part. Sci. **40**, 357 (1990).

[2] C. Ciofi degli Atti, E. Pace, and G. Salmè, Phys. Rev. C **36**, 1208 (1987); **39**, 259 (1989); **43**, 1155 (1991).

[3] C. Ciofi degli Atti, D. B. Day, and S. Liuti, Phys. Rev. C **46**, 1045 (1992); C. Ciofi degli Atti and S. Simula, *ibid.* **53**, 1689 (1996); C. Ciofi degli Atti and G. B. West, Phys. Lett. B **458**, 447 (1999).

[4] A. N. Antonov, P. E. Hodgson, and I. Zh. Petkov, *Nucleon Correlations in Nuclei* (Springer-Verlag, Berlin-Heidelberg-New York, 1993); J. B. J. M. Lanen *et al.*, Nucl. Phys. A **560**, 811 (1993); D. Van Neck, A. E. L. Dieperink, and E. Moya de Guerra, Phys. Rev. C **51**, 1800 (1995).

[5] X. Ji and J. Engel, Phys. Rev. C **40**, R497 (1989).

[6] C. Ciofi degli Atti and C. B. Mezzetti, Phys. Rev. C **79**, 051302(R) (2009).

[7] A. N. Antonov, P. E. Hodgson, and I. Zh. Petkov, *Nucleon Momentum and Density Distributions in Nuclei* (Clarendon Press, Oxford, 1988).

[8] O. Bohigas and S. Stringari, Phys. Lett. B **95**, 9 (1980).

[9] M. Jaminon, C. Mahaux, and H. Ngo, Phys. Lett. B **158**, 103 (1985).

[10] E. Moya de Guerra, P. Sarriguren, J. A. Caballero, M. Casas, and D. W. L. Sprung, Nucl. Phys. A **529**, 68 (1991); J. Martorell and E. Moya de Guerra, Ann. Phys. (NY) **158**, 1 (1984); M. Casas, J. Martorell, E. Moya de Guerra, and J. Treiner, Nucl. Phys. A **473**, 429 (1987); M. Casas, J. Martorell, and E. Moya De Guerra, Phys. Lett. B **167**, 263 (1986).

[11] A. N. Antonov, V. A. Nikolaev, and I. Zh. Petkov, Bulg. J. Phys. **6**, 151 (1979); Z. Phys. A **297**, 257 (1980); **304**, 239 (1982); Nuovo Cimento A **86**, 23 (1985); Z. Phys. A **102**, 1701 (1989); A. N. Antonov, D. N. Kadrev, and P. E. Hodgson, Phys. Rev. C **50**, 164 (1994).

[12] M. B. Barbaro, D. Berardo, R. Cenni, T. W. Donnelly, and A. Molinari, Phys. Rev. C **80**, 064320 (2009).

[13] G. B. West, Phys. Rep. **18**, 263 (1991).

[14] I. Sick, D. B. Day, and J. S. McCarthy, Phys. Rev. Lett. **45**, 871 (1980).

[15] W. M. Alberico, A. Molinari, T. W. Donnelly, E. L. Kronenberg, and J. W. Van Orden, Phys. Rev. C **38**, 1801 (1988).

[16] M. B. Barbaro, R. Cenni, A. De Pace, T. W. Donnelly, and A. Molinari, Nucl. Phys. A **643**, 137 (1998).

[17] T. W. Donnelly and I. Sick, Phys. Rev. Lett. **82**, 3212 (1999).

[18] T. W. Donnelly and I. Sick, Phys. Rev. C **60**, 065502 (1999).

[19] C. Maieron, T. W. Donnelly, and I. Sick, Phys. Rev. C **65**, 025502 (2002).

[20] A. N. Antonov, M. K. Gaidarov, D. N. Kadrev, M. V. Ivanov, E. Moya de Guerra, and J. M. Udias, Phys. Rev. C **69**, 044321 (2004).

[21] A. N. Antonov, M. K. Gaidarov, M. V. Ivanov, D. N. Kadrev, E. Moya de Guerra, P. Sarriguren, and J. M. Udias, Phys. Rev. C **71**, 014317 (2005).

[22] A. N. Antonov, M. V. Ivanov, M. K. Gaidarov, E. Moya de Guerra, P. Sarriguren, and J. M. Udias, Phys. Rev. C **73**, 047302 (2006).

[23] A. N. Antonov, M. V. Ivanov, M. K. Gaidarov, E. Moya de Guerra, J. A. Caballero, M. B. Barbaro, J. M. Udias, and P. Sarriguren, Phys. Rev. C **74**, 054603 (2006).

[24] J. A. Caballero, M. B. Barbaro, A. N. Antonov, M. V. Ivanov, and T. W. Donnelly, Phys. Rev. C **81**, 055502 (2010).

[25] S. Frullani and J. Mougey, Adv. Nucl. Phys. **14**, 1 (1984).

[26] S. Boffi, C. Giusti, F. D. Pacati, and M. Radici, Phys. Rep. **226**, 1 (1993); *Electromagnetic Response of Atomic Nuclei* (Oxford University Press, Oxford, 1996).

[27] J. J. Kelly, Adv. Nucl. Phys. **23**, 75 (1996).

[28] A. S. Raskin and T. W. Donnelly, Ann. Phys. (NY) **191**, 78 (1989).

[29] M. V. Stoitsov, A. N. Antonov, and S. S. Dimitrova, Phys. Rev. C **48**, 74 (1993).

[30] P.-O. Löwdin, Phys. Rev. **97**, 1474 (1955).

[31] A. N. Antonov, M. K. Gaidarov, M. V. Ivanov, D. N. Kadrev, G. Z. Krumova, P. E. Hodgson, and H. V. von Geramb, Phys. Rev. C **65**, 024306 (2002).

[32] J. Carbonell and V. A. Karmanov, Nucl. Phys. A **581**, 625 (1995); J. Carbonell, B. Desplanques, V. A. Karmanov, and J.-F. Mathiot, Phys. Rep. **300**, 215 (1998).

[33] J. A. Caballero, Phys. Rev. C **74**, 015502 (2006).

[34] J. J. Griffin and J. A. Wheeler, Phys. Rev. **108**, 311 (1957).

[35] M. V. Ivanov, M. B. Barbaro, J. A. Caballero, A. N. Antonov, E. Moya de Guerra, and M. K. Gaidarov, Phys. Rev. C **77**, 034612 (2008).

[36] A. N. Antonov, M. V. Ivanov, M. B. Barbaro, J. A. Caballero, E. Moya de Guerra, and M. K. Gaidarov, Phys. Rev. C **75**, 064617 (2007).

[37] J. A. Caballero, T. W. Donnelly, E. Moya de Guerra, and J. M. Udias, Nucl. Phys. A **632**, 323 (1998); **643**, 189 (1998).

[38] J. M. Udias, P. Sarriguren, E. Moya de Guerra, E. Garrido, and J. A. Caballero, Phys. Rev. C **51**, 3246 (1995); J. M. Udias, P. Sarriguren, E. Moya de Guerra, and J. A. Caballero, *ibid.* **53**, 1488 (1996).

[39] J. M. Udias, J. A. Caballero, E. Moya de Guerra, J. E. Amaro, and T. W. Donnelly, Phys. Rev. Lett. **83**, 5451 (1999).

[40] J. M. Udias, J. A. Caballero, E. Moya de Guerra, J. R. Vignote, and A. Escuderos, Phys. Rev. C **64**, 024614 (2001).

[41] M. M. Sharma, M. A. Nagarajan, and P. Ring, Phys. Lett. B **312**, 377 (1993).

[42] J. E. Amaro, M. B. Barbaro, J. A. Caballero, T. W. Donnelly, and J. M. Udias, Phys. Rev. C **75**, 034613 (2007).

[43] J. E. Amaro, M. B. Barbaro, J. A. Caballero, T. W. Donnelly, C. Maieron, and J. M. Udias, Phys. Rev. C **81**, 014606 (2010).

[44] A. M. Ankowski and J. T. Sobczyk, Phys. Rev. C **77**, 044311 (2008).

[45] Y. Horikawa, F. Lenz, and N. C. Mukhopadhyay, Phys. Rev. C **22**, 1680 (1980).

[46] E. D. Cooper, S. Hama, B. C. Clark, and R. L. Mercer, Phys. Rev. C **47**, 297 (1993).

[47] H. Nakamura, R. Seki, and M. Sakuda, Nucl. Phys. B Proc. Suppl. **139**, 201 (2005), and references therein.

[48] O. Benhar, A. Fabrocini, S. Fantoni, and I. Sick, Nucl. Phys. A **579**, 493 (1984).

[49] G. Jacob and Th. A. Maris, Rev. Mod. Phys. **45**, 6 (1973).

[50] Dipangkar Dutta, Ph.D. thesis, Northwestern University, 1999 (unpublished).